α-α correlations in nuclei above the doubly-magic ^{208}Pb nucleus

B. D. C. Kimene Kaya [1,*] T. T. Ibrahim [2,†] and S. M. Wyngaardt [1,‡]
[1]*Department of Physics, University of Stellenbosch, PO Box 1529, Stellenbosch 7599, South Africa*
[2]*Department of Physics, Federal University Lokoja, PMB 1154, Lokoja, Nigeria*

(Received 21 December 2021; accepted 4 March 2022; published 25 March 2022)

The properties of the ^{216}Rn nucleus have been investigated using α-^{212}Po and ^{8}Be-^{208}Pb systems with each interacting via a cluster model local interaction, and with a three-body α-α-^{208}Pb system within the coupled-channel formalism. The energies, transition probabilities, and cluster decay half-lives are compared with available experimental data. The two-body configurations are found to yield similar results, in fair agreement with the existing experimental data. The three-body system yields energy spectra and wave functions whose lowest energy states provides satisfactory and better description of the nucleus.

DOI: 10.1103/PhysRevC.105.034327

I. INTRODUCTION

Clustering phenomenon plays a significant role in the structure of both light and heavy nuclei [1,2]. The coexistence of the cluster degree of freedom and the mean-field in the nuclear ground state has been found as an important consideration in explaining important experimental observations [3–6]. In the simplest scenario, the binary cluster configuration provides an intuitive framework for theoretical considerations. For the more sophisticated multiple binary configurations model, one has to deal with the associated orthogonality and Pauli principle. The recent observation of a three-cluster system, though of comparable sizes in a fission process [7–9], together with the successful trinuclear theoretical description [10,11], suggest the possible existence of three-cluster modes of a nuclear system. The importance of the latter mode is seen in the three-α cluster picture of the ^{12}C Hoyle state [12–15] where the 3-α decay is considered to proceed from the S-wave motion of the $\mathrm{Be}_{\mathrm{g.s.}} + \alpha$ system owing largely to the exceptional binding character of the α particle and the weakly coupled α-α system in the $\mathrm{Be}_{\mathrm{g.s.}}$.

In the binary cluster model, important structure information has been obtained by treating heavy nuclei with masses larger than that of the doubly magic Pb isotope either as α plus ^{208}Pb or as exotic clusters plus Pb isotopes. ^{216}Rn, being one such nucleus, presents a good case for understanding how the long-range correlations leading to the formation of clusters on the nuclear surface can provide further understanding of the structure properties of nuclei. It is well known that ^{216}Rn undergoes α decay, leaving a short-lived nucleus, ^{212}Po, which in turn exhibits α-like structure on top of the double-magic nucleus ^{208}Pb, making ^{216}Rn a good candidate for a three-cluster treatment. Thus, determining whether the α-α–^{208}Pb or $^{8}\mathrm{Be}_{\mathrm{g.s.}}$-^{208}Pb configuration persists within the nuclear mean field is the focus of the current study.

In the shell-model point of view, the ground state of ^{216}Rn may be considered as four protons and four neutrons outside the doubly magic nucleus ^{208}Pb which, in compact notation, is given by $[\pi(h_{9/2})^4\nu(g_{9/2})^4]_{0^+}$, where π and ν represent the protons and neutrons. The incompletely filled outer shells, which enabled the investigation of this nucleus in the context of seniority symmetry, implies strong pairing correlations among valence nucleons, as explained in Ref. [16]. The shell-model extended to the interacting boson approximation (IBM) studies of $^{213-216}$Rn were carried out in which many isomeric states were analyzed [17]. The calculated spectroscopic properties such as the energies and the electromagnetic transitions are compared with experimental data except for the transitions in the ^{216}Rn isotope that are yet to be measured. The model predicts also the spins and parities of some experimentally ambiguous states of the radon isotopes. The narrow gap between 6_1^+ and 8_1^+ states belonging to the yrast-band observed in this mass region of even-even nuclei that is, however, not observed in the ^{216}Rn nuclei was explained as an effect of the increase in the quadrupole collectivity. Understanding the nuclear properties of this nucleus may therefore require the consideration of collective behavior involving strongly correlated nucleons on the nuclear surface.

Experimental studies using $^{208}\mathrm{Pb}(^{14}\mathrm{C}, \alpha\, 2n)^{216}\mathrm{Rn}$ and $^{208}\mathrm{Pb}(^{18}\mathrm{O}, 2\alpha\ 2n)^{216}\mathrm{Rn}$ reactions revealed a rich yrast spectrum and high-spin states in ^{216}Rn [18,19]. The results show that the nucleus possesses properties that favor vibrational interpretation as well as those of single particles. The vibrational character is seen from the alternating parity observed at high spin, above the 13^- state, characteristic of octupole collectivity [18,19]. These findings have been taken to suggest that the ^{216}Rn nucleus defines a lower mass boundary of $N = 130$ region, beyond which static intrinsic reflection-asymmetric shapes may exist in the nuclear ground state, consequence of α clustering and stable octupole shape component.

This paper attempts to determine which of the three configurations mentioned above best described the structure of ^{216}Rn. This requires a proper consideration for the α-α correlations around the nuclear surface. It is organized as follows:

*kimenekaya@sun.ac.za, kaya.christel@gmail.com
†taofiq.brahim@fulokoja.com
‡shaunmw@sun.ac.za

 ©2022 American Physical Society

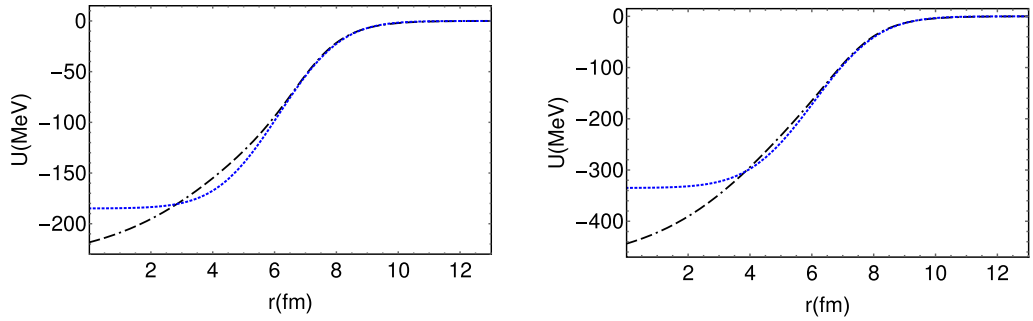

FIG. 1. Plots of the nuclear interactions for the ^{212}Po core plus ^{4}He cluster (left), and the ^{208}Pb - ^{8}Be system (right). The normalized double-folding potential and the hybrid Saxon-Woods potential are represented with dashed blue lines and dash-dotted black lines, respectively. The density distribution of the ^{8}Be is taken from the Gaussian parametrization of Ref. [29].

In Sec. II, the theoretical framework of the binary cluster model and that of the three cluster system is presented. Discussion of the results is given in Sec. III and the concluding remarks are presented in Sec. IV.

II. MODEL

A. Binary cluster system

The ^{216}Rn nucleus is first modeled as a two-body spinless systems with α-^{212}Po and ^{8}Be$_{\text{g.s.}}$-^{208}Pb as possible cluster-core systems. Here the simplest binary-cluster model (BCM) approach developed by Buck *et al.* [20,21] is considered for each configuration, and observables of good interest are compared. The stationary Schrödinger wave equation describing the relative motion of each system is given by

$$\left[-\frac{\hbar^2}{2\mu}\Delta + V(r)\right]\psi_{nJM}(\boldsymbol{r}) = E_J\psi_{nJM}(\boldsymbol{r}), \tag{1}$$

where

$$\psi_{nJM}(\boldsymbol{r}) = \frac{\varphi_{nJ}(r)}{r}Y_{JM}(\hat{\boldsymbol{r}}) \tag{2}$$

is the state wave function with corresponding energy eigenvalue E_J, and $\mu = A_1A_2/(A_1 + A_2)$ is the reduced mass of the system, where A_1 and A_2 are the mass numbers for the core and cluster, respectively. The functions $\varphi_{nJ}(r)$ and $Y_{JM}(\hat{\boldsymbol{r}})$ are the radial and the spherical harmonic wave functions. The quantities n, J, and M are, respectively, the number of nodes, the orbital and azimuthal quantum numbers. The symbol $\hat{\boldsymbol{r}} = (\theta, \phi)$ denotes the angular coordinates. Equation (1) may be reduced to the radial component of the Schrödinger wave equation for the system subject to the constraint $2n + J \geqslant G$. A good estimate of the global quantum number $G = 5A_2$ for clusters heavier than α particle is given in Ref. [21]. The quantity $V(r)$ is the total interaction between the systems comprising the nuclear $U_N(r)$ and the Coulomb $U_C(r)$ interactions. The Coulomb interaction is taken as that between two spherical nuclei given by

$$\begin{aligned} U_C(r) &= \frac{Z_1Z_2e^2}{r}, && \text{if } r \geqslant R_c \\ &= \frac{Z_1Z_2e^2}{2R_c}\left(3 - \left|\frac{r}{R_c}\right|^2\right), && \text{if } r \leqslant R_c, \end{aligned} \tag{3}$$

with the Coulomb radius R_C taken as the nuclear radius R [21]. The quantities Z_1 and Z_2, are respectively the charge numbers of the two nuclei.

The nuclear potential is in principle obtained from the double-convolution integral of the renormalized M3Y effective NN interaction with matter density distributions of the core and cluster nuclei. This is given by [22,23]:

$$U_N(r) = \lambda \iint d\boldsymbol{r}_1 d\boldsymbol{r}_2' \rho_1(\boldsymbol{r}_1)\rho_2(\boldsymbol{r}_2')g(E, |\boldsymbol{s}|), \tag{4}$$

where λ is the renormalization constant. The M3Y NN interaction is expressed as the sum of a direct finite-range and the short-range exchange terms,

$$\begin{aligned} g(E, |\boldsymbol{s}|) = 7999\frac{\exp(-4s)}{4s} - 2134\frac{\exp(-2.5s)}{2.5s} \\ - 276\left(1 - 0.005\frac{E}{A_2}\right)\delta(\boldsymbol{s}). \end{aligned} \tag{5}$$

Although the potential model yields a good account of elastic scattering and ground-state decay half-lives of α-conjugate nuclei but failed to predict the level structure of the yrast band of such system correctly. This was traced to the flat shape in the internal region of the nuclear potential, as shown in Fig. 1. However, given the successes of the Saxon-Woods interaction and its variants [22–25], a more handy approach is to construct a hybrid potential of Saxon-Woods (SW + SW^3) type given by [22]

$$U_N(r) = -V_0\left[\frac{x}{1 + \exp\left(\frac{r-R}{a}\right)} + \frac{1-x}{\left[1 + \exp\left(\frac{r-R}{3a}\right)\right]^3}\right], \tag{6}$$

with fitted parameters for different configurations. The depth V_0, the mixing parameter x, the nuclear radius R, and the diffuseness a for the α-core and the Be-core systems are listed in Table I. The fitted parameters are obtained by following the procedure described in Refs. [22,23,26], where the depth V_0 has been renormalized by fitting to the 2^+ state of ^{216}Rn. In obtaining these parameters the matter densities of the double folding interactions for the cluster-core combinations are taken from Refs. [26–29]. The two-parameter Fermi form

$$\rho_1(r_1) = \frac{\rho_0}{1 + \exp\left(\frac{r-c}{a}\right)}, \tag{7}$$

TABLE I. The fitted potential parameters for the SW[3] nuclear potential.

Partitions	V_0 (MeV)	a (fm)	x	R (fm)
α-$^{212}_{84}$Po	237.1	0.730	0.340	6.839
^{8}Be-$^{208}_{82}$Pb	485.0	0.707	0.200	6.947

with $c = 1.07A_1^{1/3}$ fm and $a = 0.54$ fm, was used for the core nuclei while the cluster densities were calculated using the Gaussian function

$$\rho_2(r_2) = \alpha \exp(-\beta r^2), \tag{8}$$

with parameters $\alpha = 0.4299$ fm^{-3} and $\beta = 0.7024$ fm^{-2} for the alpha cluster [28]. For the ^{8}Be cluster we take $\alpha = 0.602$ fm^{-3} and $\beta = 0.560$ fm^{-2} [29], where the density has been appropriately normalized by treating the nucleus as a single system rather than weakly bound two-alpha systems. Figure 1 clearly illustrates the difference in the internal region of the potentials.

The in-band electromagnetic transitions $B(E2; J' \to J)$ and quadrupole moments $Q(J)$, which are good tests of theoretical models, are given by

$$B(E2; J' \to J) = \frac{5}{4\pi}\beta_2^2 \langle J'020|J0\rangle^2 |\langle \varphi_J|r^2|\varphi_{J'}\rangle|^2,$$
$$Q(J) = -\beta_2 \frac{2J}{2J+3}\langle \varphi_J|r^2|\varphi_J\rangle \tag{9}$$

where the charge-dependent factor β_2 is expressed as

$$\beta_2 = \frac{Z_1A_2^2 + Z_2A_1^2}{(A_1 + A_2)^2}. \tag{10}$$

The decay half-life considered as an important indicator of the clustering signature is defined as [20]

$$T_{1/2} = \frac{1}{P}\frac{2\mu \ln 2}{\hbar}\exp\left[2\int_{r_2}^{r_3} k(r)dr\right]\int_{r_1}^{r_2}\frac{dr}{k(r)}, \tag{11}$$

where r_1, r_2, and r_3 are the turning points for which $V(r) = E_J$. The factor P is the probability for a preformed cluster to exist inside the parent nucleus, and the local wave number $k(r)$, is given by

$$k(r) = \sqrt{\frac{2\mu}{\hbar^2}|E_J - V(r)|}. \tag{12}$$

B. Orbit-orbit coupling of cluster systems

In the present section, ^{216}Rn is treated as a three-body system with two α particles orbiting around the ^{208}Pb core, as illustrated in Fig. 2. Following the model developed for odd-mass parent nuclei and even-even nuclei [30–37], the α particles are assumed to occupy orbits relative to ^{208}Pb corresponding to the lowest degenerate levels of ^{212}Po. The Pauli principle is satisfied by excluding nucleons of an α particle from orbitals above the ^{208}Pb Fermi surface already occupied by those of the other α particle. Assume that the systems remain in their respective ground-states such that the total Hamiltonian describing the dynamic of the problem may

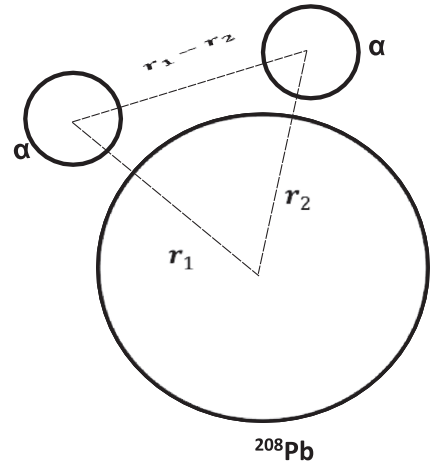

FIG. 2. A schematic diagram of the three-body configuration showing the position vectors for α-α-^{208}Pb system.

be written in the weak-coupling limit as

$$\mathcal{H} = \mathcal{H}(\boldsymbol{r}_1) + \mathcal{H}(\boldsymbol{r}_2) + V(\boldsymbol{r}_1, \boldsymbol{r}_2), \tag{13}$$

where the term $\mathcal{H}(\boldsymbol{r}_i)$ are the Hamiltonians accounting for the relative motion of each α particle around the core ^{208}Pb. The term $V(\boldsymbol{r}_1, \boldsymbol{r}_2)$ represents the interaction between the two α-particle relative motions which mixes together the various combinations of the two-α orbital motion states coupled to the total angular momentum J of the parent nucleus. The problem is thus reduced to a numerically solvable equation of motion capable of describing the properties of the heavy ^{216}Rn nuclei.

C. The basis states

In the coupled-channel approximation, the state vectors of good quantum number J in the weak-coupling limit which diagonalizes the Hamiltonian may be constructed by coupling the cluster-orbit degenerate states of both α-^{208}Pb cluster configurations. These degenerate states are in turn obtained by coupling the 0^+ state of ^{208}Pb to the orbital motion of the α particle. Thus, the basis state is formed from the coupled orbital motion as

$$|J_1J_2; JM\rangle = \sum_{M_1M_2}\langle J_1M_1J_2M_2|JM\rangle \psi_{n_1J_1M_1}(\boldsymbol{r}_1)\psi_{n_2J_2M_2}(\boldsymbol{r}_2), \tag{14}$$

where $\langle J_1M_1J_2M_2|JM\rangle$ are the Clebsch-Gordon coefficients. The states functions, $\psi_{n_iJ_iM_i}(\boldsymbol{r}_i)$ describing the relative motion satisfy the eigenvalue problem in Eq. (1).

For each value of the angular momentum J, the energies and the corresponding eigenstates $|JM\rangle$ of the full Hamiltonian given in Eq. (13) are obtained by expanding in terms of the basis states as

$$|JM\rangle = \sum_{J_1J_2} C^J_{J_1J_2}|J_1J_2; JM\rangle, \tag{15}$$

where $C^J_{J_1J_2}$ are the coefficients of expansion such that $\sum |C^J_{J_1J_2}|^2 = 1$. The sum in Eq. (15) runs over various possible combinations of angular momenta restricted by the selection rule to yield J. Hence the matrix element of $\mathcal{H}$ in the basis

state $|J_1J_2;JM\rangle$ [defined in Eq. (14)] is given by

$$\begin{aligned}&\langle J_1J_2;JM|\mathcal{H}|J_1'J_2';J'M'\rangle\\&\quad=\delta_{JJ'}\delta_{MM'}\big[\delta_{J_1J_1'}\delta_{J_2J_2'}\big(E_{J_1}+E_{J_2}\big)\\&\qquad+\langle J_1J_2;JM|V(1,2)|J_1'J_2';J'M'\rangle\big]\cdot\end{aligned}\tag{16}$$

The matrix-element $\langle J_1J_2;JM|V(1,2)|J_1'J_2';J'M'\rangle$ thus acts as a correction term to lift the degeneracy of the unperturbed energy, $E_{J_1}+E_{J_2}$ for the two-α particles with total angular momentum $|J_1-J_2|\leqslant J\leqslant J_1+J_2$. These are simple eigenvalue equations that can now be straightforwardly diagonalized to yield the energy-eigenvalues E_J corresponding to the expansion coefficients $C^J_{J_1J_2}$. The energies E_{J_i} can in principle be obtained by solving the relative motion equation for α-^{208}Pb system. For convenience, their values are taken from the well-known spectrum of ^{212}Po for both the positive-parity ground-band and the negative-parity band. However, the equation is solved to obtain the necessary wave functions in order to evaluate the matrix elements of the Hamiltonian, the electromagnetic transitions, and the moments.

D. The interacting potential

The potential $V(\boldsymbol{r}_1,\boldsymbol{r}_2)$ is taken as a sum of the finite-range nuclear and the Coulomb interactions,

$$V(\boldsymbol{r}_1,\boldsymbol{r}_2)=V_N(|\boldsymbol{r}_1-\boldsymbol{r}_2|)+V_C(|\boldsymbol{r}_1-\boldsymbol{r}_2|)\cdot\tag{17}$$

For the nuclear interaction, the low-energy four-parameter Ali-Bodmer phenomenological potential is adopted [38]. It has a Gaussian shape and is parametrized as

$$\begin{aligned}V_N(|\boldsymbol{r}_1-\boldsymbol{r}_2|)=V_r&\exp\big(-\mu_r^2|\boldsymbol{r}_1-\boldsymbol{r}_2|^2\big)\\&-V_a\exp\big(-\mu_a^2|\boldsymbol{r}_1-\boldsymbol{r}_2|^2\big),\end{aligned}\tag{18}$$

where V_r and V_a represent the strengths of the repulsive and the attractive components respectively, while μ_r and μ_a correspond to inverse ranges. These four parameters had been determined to fit the phase shifts of α-α scattering. For the Coulomb part, we choose the interaction between two spherically charged particles

$$V_C(|\boldsymbol{r}_1-\boldsymbol{r}_2|)=\frac{4e^2}{|\boldsymbol{r}_1-\boldsymbol{r}_2|}\cdot\tag{19}$$

Choosing the center of mass of the core as the coordinate origin, and since the α-α interaction being a scalar operator (tensor of rank $k=0$), the multipole expansion within a set of complete functions yields

$$V(|\boldsymbol{r}_1-\boldsymbol{r}_2|)=\sum_\lambda V_\lambda(r_1,r_2)Y_\lambda(\hat{\boldsymbol{r}}_1)\cdot Y_\lambda(\hat{\boldsymbol{r}}_2),\tag{20}$$

where the multipole component is given by

$$V_\lambda(r_1,r_2)=U_{N\lambda}(r_1,r_2)+U_{C\lambda}(r_1,r_2)\cdot\tag{21}$$

The nuclear component is defined as

$$U_{N\lambda}(r_1,r_2)=2\pi\int_{-1}^{1}V_N(|\boldsymbol{r}_1-\boldsymbol{r}_2|)P_\lambda(\cos\theta_{12})d(\cos\theta_{12}),\tag{22}$$

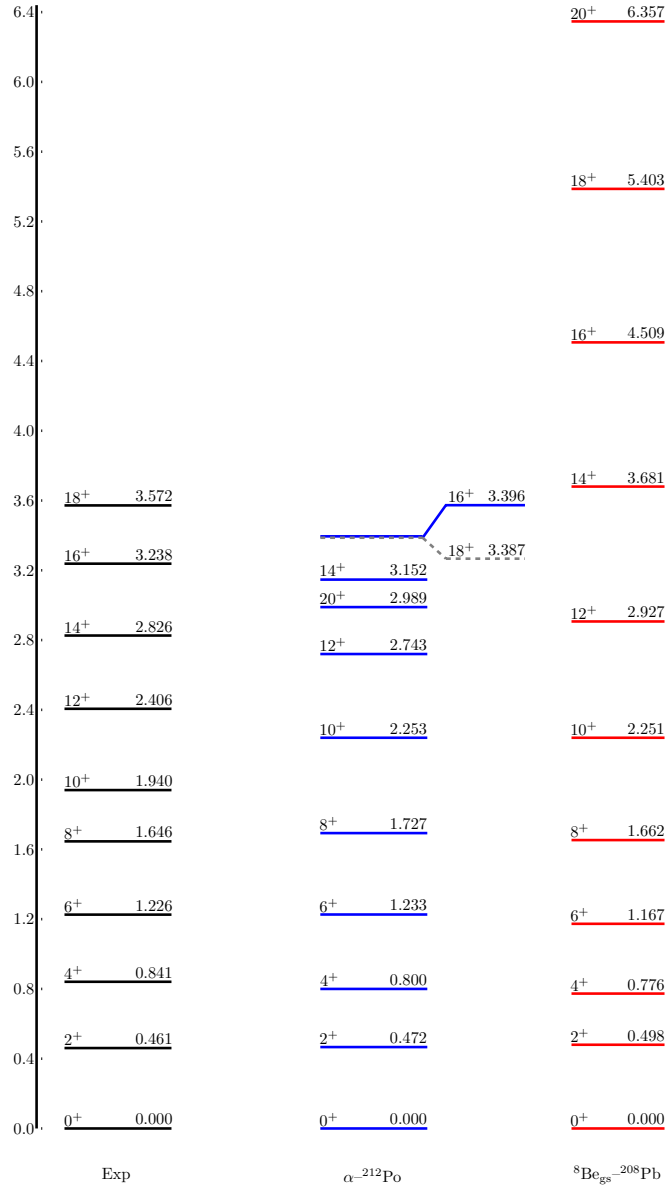

FIG. 3. Experimental and calculated positive-parity energy levels of $^{216}_{86}$Rn in MeV. Experimental data are taken from Refs. [18,19,39].

with θ_{12} being the angle between $\boldsymbol{r}_1$ and $\boldsymbol{r}_2$ and the relative distance is given by

$$|\boldsymbol{r}_1-\boldsymbol{r}_2|=\sqrt{r_1^2+r_2^2-2r_1r_2\cos\theta_{12}}\cdot\tag{23}$$

For the Coulomb component,

$$U_{C\lambda}(r_1,r_2)=4e^2\frac{r_2^\lambda}{r_1^{\lambda+1}},\tag{24}$$

with the assumption that $r_1>r_2$ so that the ratios may converge. Therefore, the matrix element of the interaction given in Eq. (17) within the basis states defined in Eq. (14) is

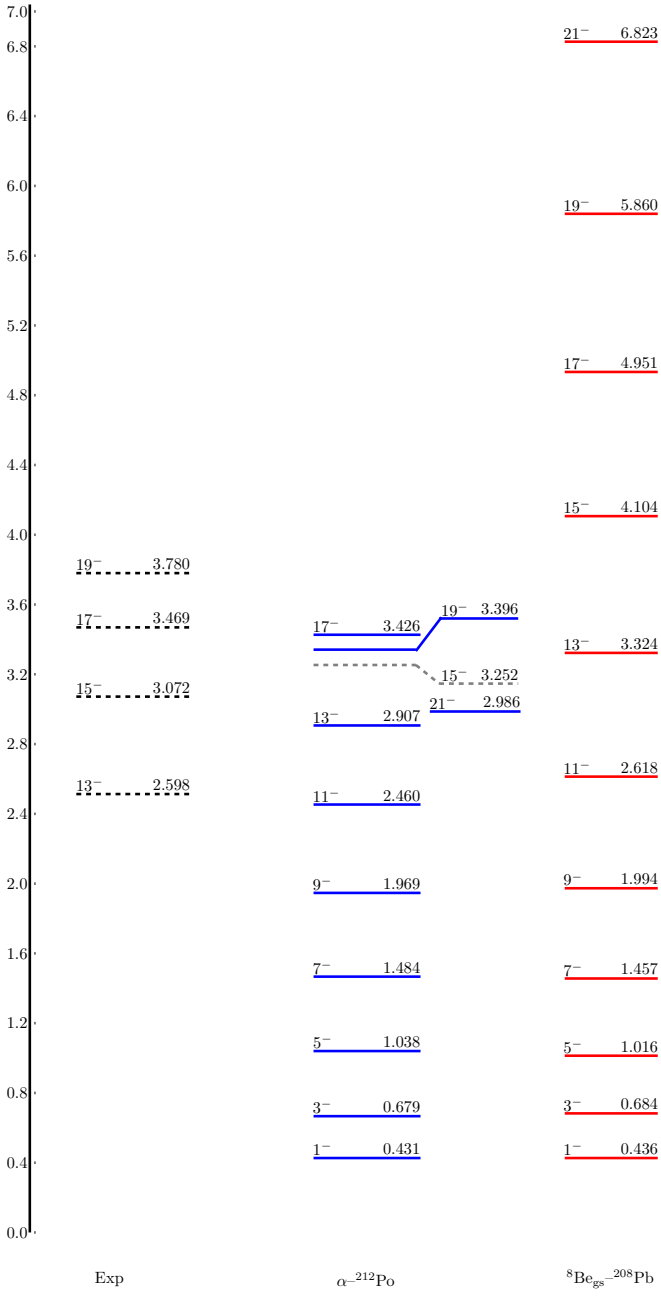

FIG. 4. Experimental and calculated negative-parity energy spectrum of $^{216}_{86}$Rn in MeV.

expressed as

$$\langle J_1 J_2; JM|V(|\boldsymbol{r}_1 - \boldsymbol{r}_2|)|J_1' J_2'; J'M'\rangle = \sum_\lambda \frac{F^\lambda}{4\pi}(-1)^{J-J_1+J_1'} \frac{\hat{J}_1\hat{J}_2\hat{J}_1'\hat{J}_2'}{2\lambda+1} W(J_1 J_1' J_2 J_2'; \lambda J) \times \langle J_1 0 J_1' 0|\lambda 0\rangle \langle J_2 0 J_2' 0|\lambda 0\rangle \delta_{JJ'}\delta_{MM'}, \quad (25)$$

where the Slater integrals F^λ [31], expressing the strength of the interaction, are written as

$$F^\lambda = \frac{2\lambda+1}{4\pi} \iint dr_1 dr_2 \varphi_{n_1 J_1}(r_1)\varphi_{n_2 J_2}(r_2) V_\lambda(r_1, r_2)\varphi_{n_1' J_1'}(r_1) \times \varphi_{n_2' J_2'}(r_2), \quad (26)$$

TABLE II. Calculated electromagnetic transition $B(E2\downarrow)$ probabilities in units of e^2 fm^4.

J_i	J_f	α-^{212}Po	^{8}Be$_{g.s.}$-^{208}Pb	Ref. [17]
2^+	0^+	372.25	1418.55	2199.31
4^+	2^+	518.53	2021.12	3126.71
6^+	4^+	538.73	2196.51	3133.72
8^+	6^+	515.64	2253.77	744.55
10^+	8^+	467.14	2253.08	239.51
12^+	10^+	403.26	2215.47	
14^+	12^+	329.20	2150.61	
16^+	14^+	249.63	2066.88	
18^+	16^+		1962.29	

with $\varphi_{n_i J_i}(r_i)$ $(i = 1, 2)$ being the relative motion wave functions corresponding to the respective initial and final states. The symbol $\hat{J} = \sqrt{2J+1}$ and the quantity $W(J_1 J_1' J_2 J_2'; \lambda J)$ is the Racah coefficients. Here, only the contributions $\lambda = 0, 2$, are retained which means that only the monopole and quadrupole components of the interaction are considered.

E. Electromagnetic properties

It is well known that the dynamic moments or electromagnetic transitions connecting different states and the static moments which account for the electric and magnetic properties of individual states are significant tools for describing the charge distributions and thus the nuclear shape. The explicit form for the multipole operator from each of the α-core contributions may be written as

$$Q_{\lambda\mu}(\boldsymbol{r}_1, \boldsymbol{r}_2) = Q_{\lambda\mu}(\boldsymbol{r}_1) + Q_{\lambda\mu}(\boldsymbol{r}_2), \quad (27)$$

where

$$Q_{\lambda\mu}(\boldsymbol{r}_i) = e\beta_\lambda r_i^\lambda Y_{\lambda\mu}(\hat{\boldsymbol{r}}_i), \quad (28)$$

with

$$\beta_\lambda = \frac{Z_1 A_2^\lambda + (-)^\lambda Z_2 A_1^\lambda}{(A_1 + A_2)^\lambda}. \quad (29)$$

Using the wave functions in the form of Eq. (15), the reduced matrix elements of the operator, $Q_{\lambda\mu}$, defines the transition

TABLE III. Calculated electromagnetic quadrupole moments $Q(J_i)$ in units of e fm^2.

J_i	α-^{212}Po	^{8}Be$_{g.s.}$-^{208}Pb	Ref. [17]
2^+	−39.16	−76.45	−62.9
4^+	−49.36	−97.04	−89.0
6^+	−53.46	−106.32	−104.6
8^+	−55.14	−111.30	−113.5
10^+	−55.56	−114.13	−129.8
12^+	−55.38	−115.70	
14^+	−54.93	−116.43	
16^+	−54.52	−116.59	
18^+	−54.40	−116.33	

probability

$$B(E\lambda; J' \to J) = \left(\frac{\hat{J}}{\hat{J}'}\right)^2 \Bigg| \sum_{J_1 J_2 J_1' J_2'} C^{J}_{J_1 J_2} C^{J'}_{J_1' J_2'} [(-)^{J+J_1'-\lambda-J_2} \hat{J}' \hat{J}_1 W(J_1 J_1' J J'; \lambda J_2) \langle J_1 \| Q_\lambda(\boldsymbol{r}_1) \| J_1' \rangle \delta(J_2, J_2')$$

$$+ (-)^{J+J_2'-\lambda-J_1} \hat{J}' \hat{J}_2 W(J_2 J_2' J J'; \lambda J_1) \langle J_2 \| Q_\lambda(\boldsymbol{r}_2) \| J_2' \rangle \delta(J_1, J_1')] \Bigg|^2, \tag{30}$$

where the matrix element

$$\langle J_i \| Q_\lambda(\boldsymbol{r}_i) \| J_i' \rangle = \frac{e\beta_\lambda}{\sqrt{4\pi}} (-1)^\lambda \hat{\lambda} \frac{\hat{J}_i'}{\hat{J}_i} \langle J_i' 0 \lambda 0 | J_i 0 \rangle \int dr_i r_i^\lambda \varphi_{n_i J_i}(r_i) \varphi_{n_i' J_i'}(r_i). \tag{31}$$

The quadrupole moment $Q(J)$ is defined as

$$Q(J) = \sqrt{\frac{16\pi}{(2\lambda+1)}} \frac{\langle JJ\lambda 0 | JJ \rangle}{\sqrt{2J+1}} \sum_{J_1 J_2} \left(C^{J}_{J_1 J_2}\right)^2 [(-)^{J+J_1-\lambda-J_2} \hat{J} \hat{J}_1 W(J_1 J_1 J J; \lambda J_2) \langle J_1 \| Q_\lambda(\boldsymbol{r}_1) \| J_1 \rangle$$

$$+ (-)^{J+J_2-\lambda-J_1} \hat{J} \hat{J}_2 W(J_2 J_2 J J; \lambda J_1) \langle J_2 \| Q_\lambda(\boldsymbol{r}_2) \| J_2 \rangle]. \tag{32}$$

III. RESULTS AND DISCUSSIONS

A. Binary cluster model

The structure of the ^{216}Rn nucleus is currently interpreted as being composed of the collective ground-state band terminating at the 8^+ state, the single-particle 10^+ state placed at about 1.940 MeV and the levels above the 10^+ state exhibiting reflection asymmetric structure. However, members of the ground state band and the levels above the observed 10^+ state seem to exhibit harmonic-like structure with ≈0.4 MeV energy spacing. This suggests that the 10^+ state member of the collective band may exist slightly above 2 MeV. Thus, treating all the positive-parity states connected by $E2$ transitions as members of the ground-state band, with the exception of the 10^+ state taken to be generated from the single-particle couplings, members of the band are predicted using both the α-^{212}Po and ^{8}Be$_{\text{g.s.}}$-^{208}Pb configurations. Figure 3 displays the spectrum of ^{216}Rn modeled with the different two-body systems interacting via SW + SW^3 local potential. Although the α-^{212}Po system appears to give better predictions of the harmonic-like structure with predicted energies lying within the observed energy range. The two configurations generate similar level schemes for the low-lying states up to the 8^+ state in fair agreement with the measured values [18,19,39]. The collective 10^+ state is predicted at ≈2.25 MeV by both configurations respectively. Above the 10^+ state however the α-^{212}Po system is seen to generate compressed and inverted states while the other configuration generates a stretched spectrum, in clear disagreement with the observed spectrum.

The negative-parity partner bands calculated with odd-G quantum number and parity-dependent interaction strengths [40] are shown in Fig. 4. The bands are calculated with a slightly deeper strength $V_0^- = 1.01V_0$ obtained from a fit to the experimental 17^- state and radius adjusted to $R = 7.019$ fm for the α-^{212}Po system. A shallower depth $V_0^- = 0.967V_0$, appropriately tuned to generate ordered states, was used for the ^{8}Be$_{\text{g.s.}}$-^{208}Pb system. The configurations are seen to give similar predictions between the 1^- bandhead and the 9^- state. Above the 9^- state the predicted structures behave differently and each mimics the structures predicted by their positive-parity partner bands. One may thus view

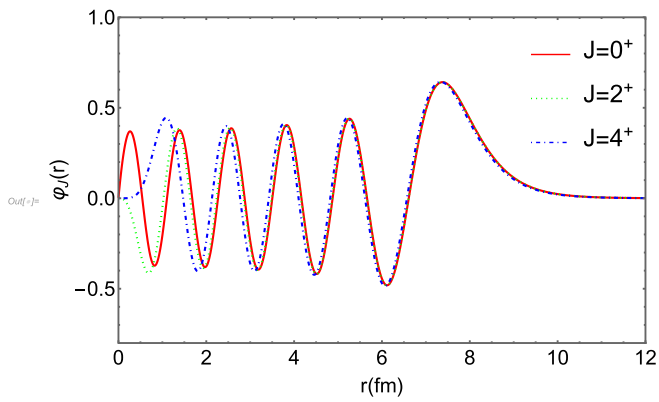

FIG. 5. Relative motion wave functions corresponding to $J = 0^+$, 2^+, and 4^+ angular momenta of the ^{4}He -^{212}Po system.

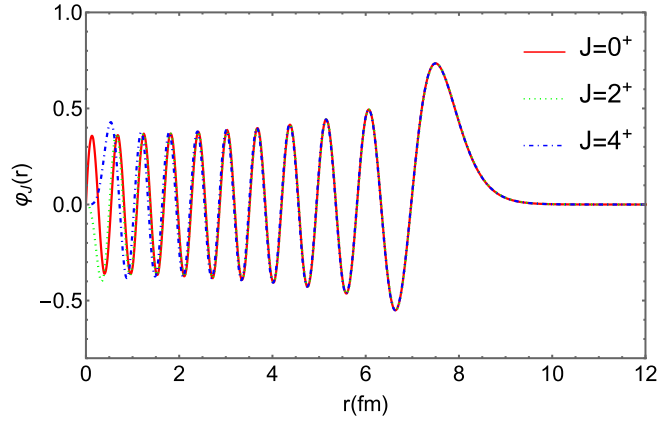

FIG. 6. Relative motion wave functions corresponding to $J = 0^+$, 2^+, and 4^+ angular momenta of the ^{8}Be$_{\text{g.s.}}$-^{208}Pb system.

TABLE IV. Calculated electromagnetic quadrupole $B(E2\downarrow)$ and dipole $B(E1\downarrow)$ transition probabilities for the negative-parity band.

	$B(E2; J \to J-2)\ e^2\ \mathrm{fm}^4$		$B(E1; J \to J-1)\ e^2\ \mathrm{fm}^2$	
J_i^π	α-^{212}Po	^{8}Be$_{\mathrm{g.s.}}$-^{208}Pb	α-^{212}Po	^{8}Be$_{\mathrm{g.s.}}$-^{208}Pb
1^-			0.25	1.339
3^-	539.28	1776.43	0.35	1.633
5^-	609.27	2071.90	0.39	1.679
7^-	605.27	2171.93	0.42	1.663
9^-	566.48	2193.13	0.44	1.620
11^-	506.33	2170.68	0.47	1.561
13^-	432.59	2117.15	0.48	1.491
15^-	350.83	2039.57	0.50	1.412
17^-	264.70	1942.47	0.52	1.326
19^-	176.68	1829.12	0.55	1.233
21^-	85.47	1702.09	0.59	1.136

the observed results as being mostly from one of the cluster-model configurations with admixture from other possible configurations.

The electromagnetic properties for the positive-parity bands are given in Tables II and III. The reduced transition strengths $B(E2\downarrow)$ [$=B(E2; J \to J-2)$] and the static moments $Q(J)$ are calculated without an effective charge. Due to the unavailability of experimental data, the results are compared with predictions from shell-model calculations [17] where however large effective charge is used. The $B(E2\downarrow)$ values obtained with ^{8}Be$_{\mathrm{g.s.}}$-^{208}Pb system are seen to be approximately four times larger than those calculated from the α-^{212}Po system. Similarly, the $Q(J)$ values of the former are also a factor of $\approx$2 greater than those of the latter. These are understood as the increase in the charge distribution with cluster size. The surface character and the number of nodes of the wave functions, shown in Figs. 5 and 6 for the lowest states, explain the predicted large values of the transitions and the variation of the $B(E2\downarrow)$ with angular momentum. The predicted transitions in both configurations are also seen to follow the expected trend similar to earlier observations. While the near constant results obtained with ^{8}Be$_{\mathrm{g.s.}}$-^{208}Pb system are similar to those of ^{218}Rn exhibiting harmonic-like structure, the α-^{212}Po gives results in agreement with those of doubly closed structure plus alpha nuclei [41,42]. Also, the constant $Q(J)$ predicted by both configuration suggest a possible structural change for spins above the 8^+ state. These results seems to suggest that the ground band extends beyond the 8^+ state with the ^{8}Be$_{\mathrm{g.s.}}$-^{208}Pb system having a stronger influence, especially at higher states. The electromagnetic quadrupole $B(E2\downarrow)$ and dipole $B(E1\downarrow)$ transitions for the negative-parity bands obtained with the core-cluster systems

TABLE V. Decay half- lives for the two cluster-core systems.

Half-life	α-^{212}Po	^{8}Be$_{\mathrm{g.s.}}$-^{208}Pb
$T_{1/2}^{\mathrm{expt}}$	45 μs	
$T_{1/2}^{\mathrm{calc}}$	40 μs	8.6×10^8 s

TABLE VI. The Ali-Bodmer interaction parameters used in the present calculation [38].

Label	μ_a (fm^{-1})	V_a (MeV)	μ_r (fm^{-1})	V_r (MeV)
V_{N1}	0.35	30	0.65	125
V_{N2}	0.42	150	0.55	325

are listed in Table IV. The orders of magnitude of the $B(E2\downarrow)$ transitions are similar to those of the positive-parity bands. Their variations with spin also agree with the expected trends. The $B(E1\downarrow)$ values, however, are found to be two orders of magnitude larger than typical enhanced single-particle value of 10^{-3} W.u. We note that similar enhanced $E1$s have been observed in other nuclei or nuclear regions such as in the high-spin state of rare-earth nuclei, some light nuclei, or the low-lying transitions near closed shells [43]. The values obtained here may be explained by the large and equal number of nodes of the opposite parity state wave functions involved. It may account for the observed octupole collectivity, particularly the reflection asymmetry at high spin of ^{216}Rn [19], given the strong connection between clustering and the octupole collectivity [37,43]. The large $B(E1\downarrow)$ values, which may have been naturally suppressed by other nuclear structure effects, explain also the marked deviation of the $B(E1) : B(E2)$ ratios from the observed values in Ref. [19].

The calculated ground-state α-decay half-life $T_{\frac{1}{2}} = 40$ μs, shown in Table V, is to be compared with the measured value $T_{\frac{1}{2}} = 45$ μs [39]. The corresponding ^{8}Be$_{\mathrm{g.s.}}$ decay of ^{216}Rn $T_{\frac{1}{2}} = 8.6 \times 10^8$ s shows the stability of the nucleus against the ^{8}Be$_{\mathrm{g.s.}}$ decay. Although the half-lives have been calculated with preformation probability $P = 1$, the result is in good agreement with the findings of Ref. [44] wherein the possibility of 2α decay mode being more likely than ^{8}Be decay has been shown. Thus one may view the constituent particles of ^{8}Be as α-particle condensate located just above the Fermi sphere of ^{208}Pb nucleus. The trapped condensate in the mean-field of the spherical core ^{208}Pb may suppress the single-particle state due to the correlations induced by interaction between the α particles. However, energetics favors the successive decay of the α particles because ^{8}Be is a weakly bound system and hence the possible existence of the α-core system or systems involving more complicated configurations.

B. Three-particle systems

Here we considered the mixing of the states generated by the α-α-core systems in the presence of weak-coupling interaction as described in Sec. II B. The energies of the core nuclei are taken from the experimental spectrum of ^{212}Po. However, the only observed negative-parity state energies for ^{212}Po are $J^\pi = 11^-$ and 13^- states placed at $E = 2.411$ and 2.772 MeV, respectively. The energies of the remaining low-spin negative-parity states are taken from Ref. [45], where the coupling between the lowest 3^- excitation of the ^{208}Pb-core and the relative motion of α-core system has been used to generate the negative-parity band. Two sets of Ali-Bodmer potential parameter values denoted by V_{N1}, and V_{N2} [38] given

in Table VI have been used in the present calculations. As an illustration typical diagonalizable Hamiltonian matrices generated from Eq. (16), for the $J = 2^+$ and $J = 19^-$ states are given by

$$\mathsf{H}^{J=2} = \begin{pmatrix} E_0 + E_2 + F^0 & 0.2F^2 & -0.53F^2 \\ 0.2F^2 & E_0 + E_2 + F^0 & -0.53F^2 \\ -0.11F^2 & -0.11F^2 & 2E_0 + F^0 - 0.06F^2 \end{pmatrix}, \tag{33}$$

$$\mathsf{H}^{J=19} = \begin{pmatrix} E_{11} + E_8 + F^0 + 0.19F^2 & 0.32F^2 & -0.10F^2 \\ 0.36F^2 & E_{13} + E_6 + F^0 + 0.18F^2 & -0.10F^2 \\ -0.08F^2 & -0.08F^2 & E_{13} + E_8 + F^0 - 0.01F^2 \end{pmatrix}. \tag{34}$$

Figures 7 and 8 show the lowest energies of the predicted rich positive- and negative-parity energy spectra obtained after the diagonalization of the Hamiltonian matrices constructed for each state. The energies calculated with the two set of nuclear interaction parameters V_{N1} and V_{N2} are denoted by Cal. I and Cal. II. The repulsive strength V_r of V_{N2} has been adjusted to 190 MeV for the positive-parity states. The values computed are generally in good agreement with the experimental data when compared with the results obtained using the binary cluster approach. In particular, the expected harmonic structure is well reproduced. The missing 10^+ member of the band is also predicted close to the expected 2 MeV considering the regular harmonic structure of the nuclei with ≈0.4 MeV spacing. Energy levels above the observed single-particle 10^+ state have also been predicted within few keV from their experimental counterparts. The energies of the 13^--band negative-parity states have also been reproduced quite well, as can be seen in Fig. 8. For the negative-parity band, the good agreement is achieved by adjusting the values of the repulsive term V_r of the parameter sets V_{N1} and V_{N2} to 30 and 190 MeV, respectively, with other parameters fixed. The figure also shows the predicted values of the unknown members of the negative-parity band. It would be interesting to have the corresponding measured data.

Using the expansion coefficients $C^J_{J_1J_2}$ obtained from the diagonalized matrices and the relative motion wave functions, the reduced transition probabilities and quadrupole moments defined in Eqs. (30) and (32) are calculated numerically and the results are summarized in Tables VII and VIII for the positive-parity band. The shell-model predictions of Ref. [17] have also been included for comparison. The $B(E2\downarrow)$ values have been obtained without the effective charge and takes the same order of magnitude as for ^{4}He-^{212}Po configuration in Table II. However, values of the quadrupole moments are predicted to increase with increasing spin, consistent in magnitude and trend up to the 8^+ state with those predicted

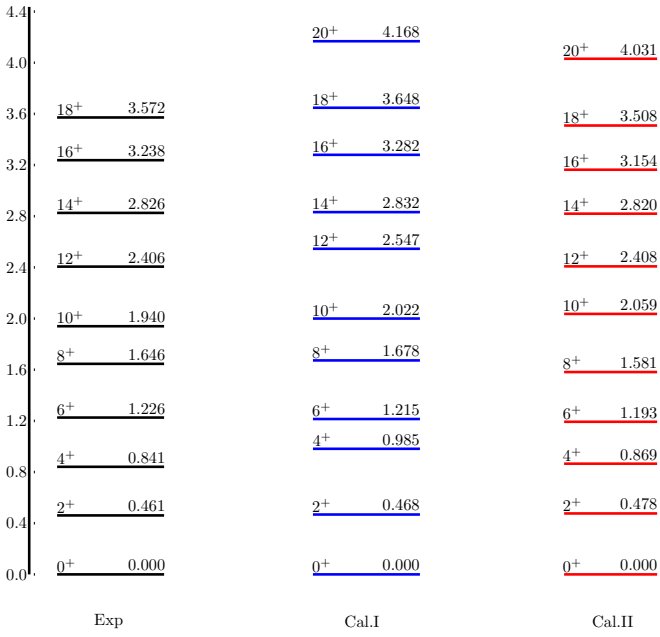

FIG. 7. Experimental and calculated positive-parity energy levels (MeV) of $^{216}_{86}$Rn obtained with $\alpha + \alpha + ^{208}$Pb system.

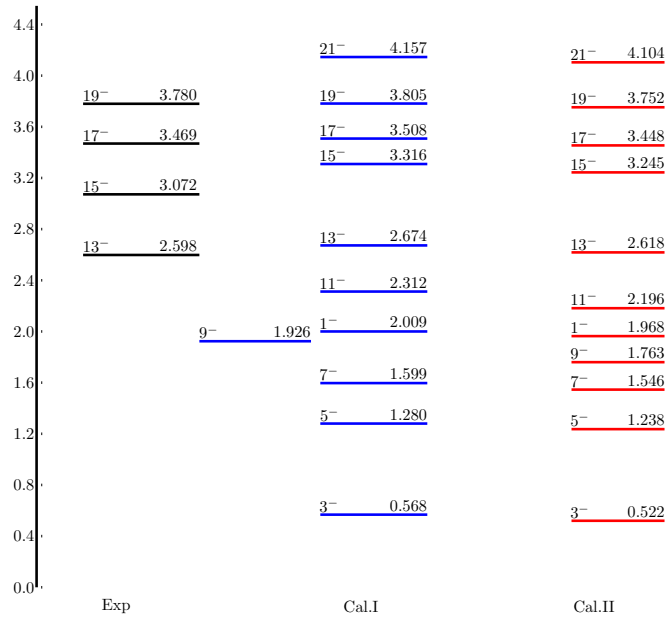

FIG. 8. Experimental and calculated negative-parity energy levels (MeV) of $^{216}_{86}$Rn obtained with $\alpha + \alpha + ^{208}$Pb system.

TABLE VII. The calculated $B(E2\downarrow)$ values in units of $e^2\,\mathrm{fm}^4$ obtained for the positive-parity transitions in the coupled orbital formalism.

J_i	J_f	Cal. I	Cal. II	Ref. [17]
2^+	0^+	562.56	368.67	2199.31
4^+	2^+	620.13	256.07	3126.71
6^+	4^+	870.08	497.34	3133.72
8^+	6^+	863.95	828.11	744.55
10^+	8^+	926.42	694.27	239.51
12^+	10^+	787.91	548.51	
14^+	12^+	493.74	614.83	
16^+	14^+	826.37	237.14	
18^+	16^+	822.77	3.13	

with the ^{4}He -^{212}Po system. The constant values predicted for spins above the 8^+ state in the latter is not observed in the present configuration. The intraband $B(E2\downarrow)$ and the dipole $B(E1\downarrow)$ transition probabilities for the negative-parity states are listed in Table IX. The predicted values may be compared with the corresponding values for the ^{4}He -^{212}Po core-cluster system presented in Table IV. In particular, the dipole transitions are seen to decrease with increasing spin and varies within three orders of magnitude in sharp contrast with the core-cluster prediction. While the predicted transitions from the low-spin states (and the 17^- state with 0.116 W.u.) agree with those of $\alpha + {}^{208}$Pb configuration which are an order of magnitude away from typical enhanced values in the mass region, the predictions for higher states are in good agreement with the enhanced range of values [43]. The calculated $B(E1\downarrow)/B(E2\downarrow)$ ratios have also been compared with the measured values of Ref. [19] in Table X, where the calculated $B(E1; 14^+ \rightarrow 13^-) = 8.39 \times 10^{-4}\ e^2\,\mathrm{fm}^2$ and $7.00 \times 10^{-6}\ e^2\,\mathrm{fm}^2$ have been used for Cal. I and Cal. II, respectively. Similarly, the values $B(E1; 16^+ \rightarrow 15^-) = 0.176\ e^2\,\mathrm{fm}^2$ and $0.194\ e^2\,\mathrm{fm}^2$ were used for the 16^+ state. This seems to show that, even though the energies are correctly predicted within the formalism and the results generally represent great improvement over the binary cluster predictions, the wave functions may still not be adequate to explain the observed transition probabilities among other features.

TABLE VIII. Calculated electromagnetic quadrupole moments in $e\,\mathrm{fm}^2$ obtained for the positive-parity transitions in the coupled orbital formalism.

J_i	Cal. I	Cal. II	Ref. [17]
2^+	−32.53	−35.83	−62.9
4^+	−48.83	−44.57	−89.0
6^+	−51.44	−51.25	−104.6
8^+	−55.09	−56.29	−113.5
10^+	−58.41	−65.74	−129.8
12^+	−65.60	−65.61	
14^+	−72.04	−71.55	
16^+	−74.96	−74.87	
18^+	−75.74	−75.74	
20^+	−75.29	−75.29	

TABLE IX. Calculated quadrupole $B(E2\downarrow)$ and dipole $B(E1\downarrow)$ transition probabilities for the negative-parity band in the coupled orbital formalism.

	$B(E2\downarrow)\ e^2\,\mathrm{fm}^4$		$B(E1\downarrow)\ e^2\,\mathrm{fm}^2$	
J_i^π	Cal. I	Cal. II	Cal. I	Cal. II
1^-			0.35	0.35
3^-	607.41	605.37	0.33	0.26
5^-	987.82	815.96	0.30	0.24
7^-	835.11	593.84	0.023	0.0016
9^-	742.65	810.20	0.057	0.051
11^-	930.72	927.75	0.0024	0.0022
13^-	531.03	528.85	0.000 11	0.0000 17
15^-	690.27	684.37	0.15	0.0022
17^-	691.89	685.83	0.26	0.27
19^-	522.21	520.12	0.000 34	0.000 36

IV. CONCLUSIONS

In summary, ^{216}Rn has been modeled in various configurations with a dominant α-particle component to account for its decay and spectroscopic properties. Satisfactory results are obtained for the ground state α-decay half-life. The excitation energies are well reproduced especially with $\alpha + \alpha + {}^{208}$Pb model treated within the coupled-channel formalism. The enhanced transition probabilities and quadrupole moments obtained show strong correlations between the configurations considered. The results show that the ^{216}Rn states could therefore be described as a mixture of $\alpha + {}^{208}$Pb and $^8\mathrm{Be}_{\mathrm{g.s.}} + {}^{208}$Pb systems for which the latter may be taken to exist for the most part as $\alpha + \alpha + {}^{208}$Pb systems due to the weakly bound nature of the $^8\mathrm{Be}_{\mathrm{g.s.}}$ ground state.

ACKNOWLEDGMENTS

B. D. C. Kimene Kaya thanks the University of Stellenbosch for granting permission to carry out this research project at the physics department. This work was partly supported by South African National Research Foundation (NRF), Grant No. 807778.

TABLE X. Experimental and calculated $B(E1\downarrow)/B(E2\downarrow)$ $10^{-6}\,\mathrm{fm}^{-2}$ transition ratios.

J_i	Expt.	Cal. I	Cal. II
14^+	0.16(3)	1.7	0.011
15^-	0.7(1)	213	3.17
16^+	0.13(3)	213	820
17^-	0.6(1)	383	388
19^-	0.05(2)	0.66	0.69

[1] M. Freer, H. Horiuchi, Y. Kanada-Enyo, D. Lee, and Ulf-G. Meiner, Rev. Mod. Phys. **90**, 035004 (2018).

[2] A. I. Budaca, R. Budaca, and I. Silisteanu, Nucl. Phys. A **951**, 60 (2016).

[3] P. Adsley, D. G. Jenkins, J. Cseh, S. S. Dimitriova, J. W. Brümmer, K. C. W. Li, D. J. Marín-Lámbarri, K. Lukyanov, N. Y. Kheswa, R. Neveling, P. Papka, L. Pellegri, V. Pesudo, L. C. Pool, G. Riczu, F. D. Smit, J. J. van Zyl, and E. Zemlyanaya, Phys. Rev. C **95**, 024319 (2017).

[4] H. J. Rose, and G. A. Jones, Nature (London) **307**, 245 (1984).

[5] S. Gales, E. Hourani, M. Hussonnois, J. P. Schapira, L. Stab, and M. Vergnes, Phys. Rev. Lett. **53**, 759 (1984).

[6] P. B. Price, J. D. Stevenson, S. W. Barwick, and H. L. Ravn, Phys. Rev. Lett. **54**, 297 (1985).

[7] Yu. V. Pyatkov, D. V. Kamanin, A. A. Alexandrov, I. A. Alexandrova, Z. I. Goryainova, V. Malaza, N. Mkaza, E. A. Kuznetsova, A. O. Strekalovsky, O. V. Strekalovsky, and V. E. Zhuchko, Phys. Rev. C **96**, 064606 (2017).

[8] Yu. V. Pyatkov, Eur. Phys. J. A **48**, 94 (2012).

[9] D. V. Kamanin, and Yu. V. Pyatkov, Lect. Notes Phys. **875**, 183 (2013).

[10] A. K. Nasirov, R. B. Tashkhodjaev, and W. von Oertzen, Eur. Phys. J. A **52**, 135 (2016).

[11] R. B. Tashkhodjaev, A. K. Nasirov, and E. Kh. Alpomeshev, Phys. Rev. C **94**, 054614 (2016).

[12] D. Jenkins, J. Phys. G **43**, 024003 (2016).

[13] D. M. Brink, J. Phys.: Conf. Ser. **111**, 012001 (2008).

[14] M. Freer, J. Phys.: Conf. Ser. **590**, 012014 (2015).

[15] B. Buck, A. C. Merchant, and S. M. Perez, Phys. Rev. C **87**, 024304 (2013).

[16] Qi Chong, Phys. Lett. B **773**, 616 (2017).

[17] K. Yanase, E. Teruya, K. Higashiyama, and N. Yoshinaga, Phys. Rev. C **98**, 014308 (2018).

[18] P. D. Cottle, M. Gai, J. F. Ennis, J. F. Shriner, S. M. Sterbenz, D. A. Bromley, C. W. Beausang, L. Hildingsson, W. F. Piel, D. B. Fossan, J. W. Olness, and E. K. Warburton, Phys. Rev. C **35**, 1939 (1987).

[19] M. E. Debray, J. Davidson, M. Davidson, A. J. Kreiner, M. A. Cardona, D. Hojman, D. R. Napoli, S. Lenzi, G. de Angelis, D. Bazzacco, S. Lunardi, M. De Poli, C. Rossi-Alvarez, A. Gadea, N. Medina, and C. A. Ur, Phys. Rev. C **73**, 024314 (2006).

[20] B. Buck, A. C. Merchant, and S. M. Perez, Phys. Rev. Lett. **65**, 2975 (1990).

[21] B. Buck, A. C. Merchant, and S. M. Perez, Phys. Rev. Lett. **76**, 380 (1996).

[22] T. T. Ibrahim, S. M. Perez, and S. M. Wyngaardt, Phys. Rev. C **82**, 034302 (2010).

[23] B. D. C. Kimene Kaya, S. M. Wyngaardt, T. T. Ibrahim, and W. A. Yahya, Phys. Rev. C **98**, 044308 (2018).

[24] M. A. Souza, H. Miyake, T. Borello-Lewin, C. A. da Rocha, and C. Frajuca, Phys. Lett. B **793**, 8 (2019).

[25] M. A. Souza and H. Miyake, Phys. Rev. C **104**, 064301 (2021).

[26] T. T. Ibrahim, S. M. Perez, S. M. Wyngaardt, B. Buck, and A. C. Merchant, Phys. Rev. C **85**, 044313 (2012).

[27] B. Hahn, D. G. Ravenhall, and R. Hofstadter, Phys. Rev. **101**, 1131 (1956).

[28] G. R. Satchler and W. G. Love, Phys. Rep. **55**, 183 (1979).

[29] V. Della Rocca, R. Bijker, and F. Iachello, Nucl. Phys. A **966**, 158 (2017).

[30] B. Buck, A. C. Merchant, and S. M. Perez, Nucl. Phys. A **644**, 306 (1998).

[31] B. Buck, A. C. Merchant, and S. M. Perez, Phys. Rev. C **58**, 2990 (1998).

[32] A. C. Merchant and A. Guglielmetti, Nucl. Phys. A **600**, 403 (1996).

[33] B. Buck, A. C. Merchant, S. M. Perez, T. T. Ibrahim, and S. M. Wyngaardt, J. Phys. G **36**, 085101 (2009).

[34] B. Buck, A. C. Merchant, and S. M. Perez, J. Phys. G **34**, 1985 (2007).

[35] B. Buck, A. C. Merchant, and S. M. Perez, J. Phys. G **35**, 085101 (2008).

[36] Y. Suzuki and S. Ohkubo, Phys. Rev. C **82**, 041303(R) (2010).

[37] T. T. Ibrahim and S. M. Wyngaardt, Phys. Rev. C **84**, 044330 (2011).

[38] S. Ali and A. R. Bodmer, Nucl. Phys. **80**, 99 (1966).

[39] S.-C. Wu, Nucl. Data Sheets **108**, 1057 (2007).

[40] B. Buck, A. C. Merchant, and S. M. Perez, Phys. Rev. C **58**, 2049 (1998).

[41] T. T. Ibrahim, S. M. Wyngaardt, and B. D. C. Kimene Kaya, Nucl. Phys. A **966**, 73 (2017).

[42] T. T. Ibrahim, A. C. Merchant, S. M. Perez, and B. Buck, Phys. Rev. C **99**, 064332 (2019).

[43] P. A. Butler and W. Nazarewicz, Rev. Mod. Phys. **68**, 349 (1996).

[44] K. P. Santhosh and Tinu Ann Jose, Phys. Rev. C **104**, 064604 (2021).

[45] T. T. Ibrahim, Ph.D. thesis, Stellenbosch University, 2009 (unpublished).